J. Fluid Mech. (2020), vol. 894, A20. © The Author(s), 2020. Published by Cambridge University Press doi:10.1017/jfm.2020.244

894 A20-1

Lift and drag coefficients of deformable bubbles in intense turbulence determined from bubble rise velocity

Ashwanth K. R. Salibindla¹, Ashik Ullah Mohammad Masuk¹, Shiyong Tan¹ and Rui Ni¹,†

¹Department of Mechanical Engineering, Johns Hopkins University, Baltimore, MD 21210, USA

(Received 21 November 2019; revised 16 March 2020; accepted 18 March 2020)

We experimentally investigate the rise velocity of finite-sized bubbles in turbulence with a high energy dissipation rate of $\epsilon \gtrsim 0.5~\text{m}^2~\text{s}^{-3}$. In contrast to a 30–40% reduction in rise velocity previously reported in weak turbulence (the Weber number (*We*) is much smaller than the Eötvös number (*Eo*); $We \ll 1 < Eo$), the bubble rise velocity in intense turbulence shows a surprising new behaviour: an abrupt transition from an order of magnitude slower to a factor of two faster than rising in an otherwise quiescent medium. This transition occurs when *We* increases from below one to above one, underscoring the key role played by the turbulence-induced deformation. We also formulate a model based on bubble–eddy coupling, and the results show an excellent agreement with not only our data in intense turbulence but also other works on weak turbulence. The model also helps us to extract the lift and drag coefficients of bubbles in intense turbulence for a wide range of *We* and Reynolds numbers *in situ*.

Key words: bubble dynamics, multiphase flow, isotropic turbulence

1. Introduction

Leonardo da Vinci's famous drawing of bubbles entrained in turbulent water as it falls from a sluice into a pool clearly depicts a sophisticated interaction between organized turbulence structures and bubbles. This complex interaction has inspired decades of seemingly parallel research on (i) coherent structures, which are often described as 'eddies' or 'vortices', in turbulence (She, Jackson & Orszag 1990) and (ii) the non-rectilinear rising motion of finite-sized deformable bubbles (Magnaudet & Eames 2000; Mougin & Magnaudet 2001; Ern *et al.* 2012). Although each subject represents a complex problem in and of itself, the coupling between them (Lohse 2018; Mathai, Lohse & Sun 2020) – especially as bubbles become deformed by the nearby turbulent eddies – poses formidable challenges in relation to many applications, including aerobic reactors (Kawase & Moo-Young 1990) and bubble-mediated gas transfer in the ocean (Woolf 1997; Boettcher, Fineberg & Lathrop 2000).

In turbulence, the bubble-vortex interaction is known to affect the ensemble-averaged mean bubble rise velocity $\langle w_b \rangle$. Wang & Maxey (1993) showed that $\langle w_b \rangle$

of micro-bubbles in forced isotropic turbulence decreases by 33% when compared to that in an otherwise quiescent medium, and this difference was attributed to bubbles being trapped in high-vorticity, low-pressure vortex cores. Spelt & Biesheuvel (1997) proposed a different mechanism, suggesting that bubbles tend to preferentially sample the downward flows in turbulence, which effectively reduces $\langle w_b \rangle$ by up to 50%. In addition to these simulation results, similar experimental studies were also carried out by measuring $\langle w_b \rangle$ in water tunnels driven by passive (Aliseda & Lasheras 2011) or active (Poorte & Biesheuvel 2002; Prakash *et al.* 2012) grids. Despite the difference in bubble sizes (0.5–1.5 mm), the findings are both qualitatively and quantitatively consistent with the numerical results. These results support the notion that $\langle w_b \rangle$ decreases due to either vortex trapping or preferential sampling.

Bubbles travelling in turbulence are subjected to multiple hydrodynamic forces including buoyancy, drag, lift, added mass, Basset history and pressure forces (Sridhar & Katz 1995; Magnaudet & Eames 2000). It is often difficult to isolate the effects of individual forces on $\langle w_b \rangle$ from experimental results because, compared with the number of unknowns, not many quantities can be directly measured. Mazzitelli, Lohse & Toschi (2003) performed direct numerical simulations (DNS) to account for two-way couplings. By switching the lift on and off, they demonstrated that the addition of lift enhances the probability of bubbles preferentially sampling downward flows in turbulence. When lift was turned off, bubbles accumulated at the centre of the eddies (Wang & Maxey 1993).

Loisy & Naso (2017) conducted a DNS of deformable bubbles rising in turbulence. Their work confirmed the earlier results obtained by Wang & Maxey (1993) and Spelt & Biesheuvel (1997), indicating that both preferential sampling and vortex trapping play roles in determining the bubble rise velocity. Furthermore, they suggested that the velocity ratio $\beta = u'/\langle w_b \rangle$ (u' is the turbulent fluctuation velocity) determines which mechanism is at play. The reduction in velocity is primarily driven by preferential downward sampling for $\beta < 1$, whereas vortex trapping dominates for $\beta > 1$.

Most prior studies have focused on understanding the bubble dynamics in high- Re_{λ} turbulence ($Re_{\lambda} = u'\lambda/\nu$), where λ is the Taylor microscale and ν is the kinematic viscosity. Here u' is the velocity scale that is typically associated with eddies of size L (the integral length scale) (Frisch 1995). However, bubbles with size D in the inertial subrange ($\eta \ll D \ll L$, where η is the Kolmogorov length scale) interact more frequently with eddies of a similar size D rather than with flow structures much larger or much smaller. Based on this argument, a more relevant velocity scale would be the eddy velocity scale at the bubble size: $u_D \sim (\epsilon D)^{1/3}$ (Frisch 1995). In most previous experiments conducted in systems with small ϵ , the bubble rise velocity $\langle w_b \rangle$ is much larger than u_D , which indicates that the bubble dynamics is primarily dominated by buoyancy rather than by turbulence.

The main objective of this paper is to experimentally study $\langle w_b \rangle$ of finite-sized bubbles in a different regime, namely $\langle w_b \rangle / u_D \lesssim 1$. It happens that, in this regime, bubble deformation induced by turbulence starts to become important. In § 2, the relevant dimensionless numbers are introduced and explained. In § 3, we provide in-depth discussions of our experimental set-up and our two-phase simultaneous measurements. Details concerning the data analysis process and a simple model are then addressed in § 4. In particular, we describe how we extract the lift and drag coefficients of deforming bubbles in turbulence.

2. Dimensionless numbers

The first dimensionless number that comes to mind for virtually any fluid dynamics problems is the Reynolds number, more specifically the Taylor-scale Reynolds number R_{λ} as is customary in homogeneous and isotropic turbulence. Parameter R_{λ} sets the scale separation between L and η . In the context of bubble dynamics in turbulence, as long as R_{λ} is large enough so that $\eta \ll D \ll L$ is satisfied, R_{λ} is not important.

For bubbles with $\langle w_b \rangle/u_D \lesssim 1$, turbulence stresses turn out to be sufficiently large to deform bubbles. The key dimensionless number for quantifying deformation is the Weber number, $We = 2.13 \rho (\epsilon D)^{2/3} D/\sigma$ (2.13 is the Kolmogorov constant for the second-order longitudinal structure function), which measures the ratio between the dynamic pressure gradients and the restoring Laplace pressure driven by the surface tension (Kolmogorov 1949; Hinze 1955). When $We \gtrsim 1$, the turbulence-induced deformation starts to become important. Meanwhile, given that we focus primarily on air bubbles in water with large density difference between the two phases, the buoyancy-induced deformation, measured by the Eötvös number $Eo = \Delta \rho g D^2/\sigma$, could also be important.

For weak turbulence (small ϵ ; $\epsilon \ll 0.5$ m² s⁻³), millimetre-sized bubbles are either solely deformed by buoyancy, $Eo > 1 \gg We$, or completely spherical, $1 > Eo \gg We$. Since $We \sim D^{5/3}$, We can be larger than one for large centimetre-sized bubbles, which may lead to a conclusion that the turbulence-induced deformation can still be important in weak turbulence. However, $Eo \sim D^2$ grows faster than We as D increases; for bubbles with We > 1 in weak turbulence, their Eo is significantly larger. For example, in turbulence with $\epsilon \approx 10^{-3}$ m² s⁻³ (Mercado et al. 2012), We becomes larger than one if D > 33 mm. At that size, Eo = 148, which is more than two orders of magnitude larger than We, indicating a dominant role played by buoyancy.

Turbulence-induced deformation starts to play a role if $We \gtrsim Eo > 1$. This relationship can actually be solved to determine the range of bubble sizes and the minimum ϵ needed: $\epsilon \gtrsim 0.57 \text{ m}^2 \text{ s}^{-3}$. Much lower than this number, bubbles will either stay spherical or be deformed primarily by buoyancy, never by turbulence, regardless of the bubble size. Throughout the rest of this paper, weak turbulence refers to turbulence with low $\epsilon \ll 0.5 \text{ m}^2 \text{ s}^{-3}$, which also means $Eo \gg We$ and $We \ll 1$. Strong turbulence represents turbulence with high $\epsilon \sim 0.5 \text{ m}^2 \text{ s}^{-3}$. At this ϵ , there will be a range of bubble sizes $(D \approx 2-3 \text{ mm})$ that satisfies the criterion of $We \approx Eo \gtrsim 1$.

It would be tempting to relate the non-dimensionalized velocity $\langle w_b \rangle / u_D$ to either We or Eo. But it is easy to show that $Eo/We = (\langle w_b \rangle / u_D)^2 / 2.13$ if $\langle w_b \rangle = \sqrt{gD}$. This relationship implies that these dimensionless groups are not independent. In other words, $\langle w_b \rangle / u_D \lesssim 1$ and $We \gtrsim Eo$ are equivalent conditions. So rather than adopting the dimensionless forms, in this paper, we decide to present $\langle w_b \rangle$ as a function of bubble physical size D. Nevertheless, the dimensionless lift and drag coefficients can still be linked to We, Eo and the bubble-scale Reynolds number Re_b .

3. Experimental facility

In this paper, as shown in figure 1, experiments were performed in the V-ONSET facility (Masuk *et al.* 2019*b*), a vertical water tunnel with an octagonal test section. The octagonal test section was designed to provide optical access to the centre of the tunnel through multiple flat surfaces (figure 1a). An array with 88 nozzles (5 mm in diameter) was fabricated using additive manufacturing and was utilized to inject high-speed water jets (up to 12 m s^{-1}) into the test section to drive turbulence. The

894 A20-4 A. K. R. Salibindla, A. U. M. Masuk, S. Tan and R. Ni

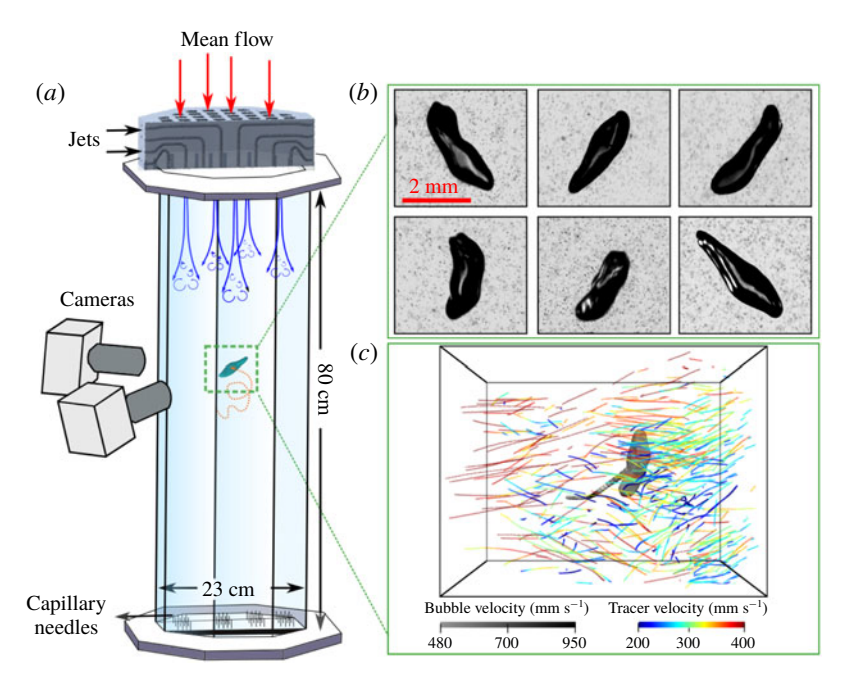


FIGURE 1. (a) Schematic of the test section of V-ONSET (Masuk *et al.* 2019b). (b) Images of a deforming bubble with surrounding tracer particles on six cameras. (c) Sample of reconstructed three-dimensional tracer tracks around a bubble (Masuk, Salibindla & Ni 2019a). The instantaneous velocity magnitudes of both the bubble and surrounding tracers are colour-coded.

resulting turbulence is close to being homogeneous and isotropic with a large energy dissipation rate $\epsilon \approx 0.5 \text{ m}^2 \text{ s}^{-3}$. The Kolmogorov length scale (η) and time scale (τ_{η}) of the system are 38 μ m and 1.4 ms, respectively. Here L is 3.2 cm and the fluctuation velocity $u' = 0.25 \text{ m s}^{-1}$. Finally, Re_{λ} is kept at around 346 in our system.

Air bubbles were injected into this system using capillary needles located at the bottom of the test section. Varying the needle size and airflow rates allows for the injection of bubbles of different sizes. These bubbles slowly rose up into the centre of the test section, where they interacted with the homogeneous isotropic turbulence generated by the jet array. In addition to the turbulence created by jets, a constant downward mean flow was employed to keep bubbles in the view area for an extended period of time. Furthermore, the carrier phase was seeded with 50 μ m tracer particles that were used to quantify local flows around bubbles. The details of this facility and its flow characteristics can be found in Masuk *et al.* (2019*b*).

The dynamics of bubbles and surrounding tracer particles were tracked by six high-speed cameras within a view volume of roughly $6 \times 6 \times 6$ cm³. These cameras are capable of recording images at 4000 frames per second with one-megapixel resolution. Each camera had a dedicated light-emitting diode panel at the opposing side across the tunnel that cast shadows of bubbles and tracer particles onto the camera imaging plane. These images, as shown in figure 1(b), were then processed to separate the two phases. Six cameras were employed primarily for accurately reconstructing bubble shape. The collected images were processed by a virtual-camera visual hull method (Masuk *et al.* 2019*a*) to optimize the geometry by enforcing constraints imposed by the surface tension. After reconstruction, we tracked the centre of mass of roughly

29 000 bubbles (an example of such is shown in figure 1c). The trajectory of each bubble, on average, consists of 360 frames. In total, about 10^7 data points of the local vertical bubble velocity $u_{z,b}$ were collected. Simultaneously, the mean volumetric flow rate of water through the tunnel was monitored by a digital flow meter, from which the mean vertical flow velocity \overline{w} , averaged over the entire cross-section, can be determined. Velocity \overline{w} has to be subtracted from $u_{z,b}$ to obtain the bubble rise velocity: $w_b = u_{z,b} - \overline{w}$.

In addition, in each frame, over 6000 tracer particles were tracked simultaneously using our in-house high-concentration particle tracking code (Tan *et al.* 2019, 2020). A snapshot of our three-dimensional reconstructed results, including both three-dimensional bubble geometry and three-dimensional tracks of surrounding tracers, is shown in figure 1(c). Within a certain search radius (SR = 1.5D-3D) from the centre of a bubble, N tracer particles can be identified (N ranges from 5 to 30 particles). Averaging the velocity of all these tracer particles $u_{z,i}$ helps to estimate the local flow velocity $u_{z,l} = \sum_{i=1}^{N} u_{z,i}/N$ at the centre of the bubble. In the governing equation ((4.1) in § 4) for bubbles (Magnaudet & Eames 2000), it is clearly stated that the fluid velocity used has to be the unperturbed ambient flow taken at the centre of a bubble if the bubble was not there. The local flow velocity $\overline{w_s}$, averaged across a small region where bubbles passed by, is found to be larger than \overline{w} for the remaining regions because rising bubbles always drag surrounding fluid with them (Liu *et al.* 2005; Lewandowski *et al.* 2018; Risso 2018). This perturbed flow $\overline{w_s}$ has to be subtracted from $u_{z,l}$ to estimate the unperturbed vertical flow velocity, i.e. $w_l = u_{z,l} - \overline{w_s}$.

4. Results and discussion

Figure 2 shows the ensemble average of bubble rise velocity $\langle w_b \rangle$ as a function of bubble size. Three groups of data, including bubbles rising in a quiescent medium (Clift *et al.* 2005), weak turbulence ($We \ll Eo$, $\epsilon = 1.3 \times 10^{-4}$ – 6×10^{-3} m² s⁻³) (Poorte & Biesheuvel 2002; Aliseda & Lasheras 2011; Prakash *et al.* 2012) and our experiments (strong turbulence, $\epsilon = 0.5$ m² s⁻³), are shown and compared to each other. For bubbles rising in a quiescent medium, $\langle w_b \rangle$ of small bubbles increases as D grows because of buoyancy. For large bubbles, the pressure drag induced by flow separation and wake formation limit $\langle w_b \rangle$. When the background flow becomes weakly turbulent, $\langle w_b \rangle$ still maintains a trend similar to that observed for bubbles rising in an otherwise quiescent medium, but the magnitude is about 30–40% smaller.

Once ϵ reaches 0.5 m² s⁻³ (We becomes important), a clear deviation from both the quiescent and weakly turbulent cases is observed; not just the magnitude, but the entire dependence of $\langle w_b \rangle$ on the bubble size D is altered. Three regimes are clearly observed: (i) $\langle w_b \rangle$ decreases by a factor of two as D grows from 0.5 mm (13.5 η) to 0.8 mm (21.3 η), as shown in the inset of figure 2; (ii) $\langle w_b \rangle$ increases by over an order of magnitude for D=0.8-2.2 mm (21.3 η -58.5 η); at 2.2 mm, $\langle w_b \rangle$ finally recovers the value in a quiescent medium; and (iii) for D=2.2-10 mm (58.5 η -266 η), $\langle w_b \rangle$ continues to grow, exceeding the bubble rise velocity in a quiescent medium, although at a reduced growth rate. In sum, $\langle w_b \rangle$ varies from a factor of 11 (small bubbles) below that in a quiescent medium to almost two times above.

The observed change of $\langle w_b \rangle$ in intense turbulence must be a result of the coupling between bubbles and surrounding turbulent flows. To estimate the nearby flow velocity, similar to $\langle w_b \rangle$, $\langle w_l \rangle$ is determined by performing an ensemble average of w_l over all bubbles of a particular size D. Figure 3(a) shows $\langle w_l \rangle$ as a function of the bubble

894 A20-6 A. K. R. Salibindla, A. U. M. Masuk, S. Tan and R. Ni

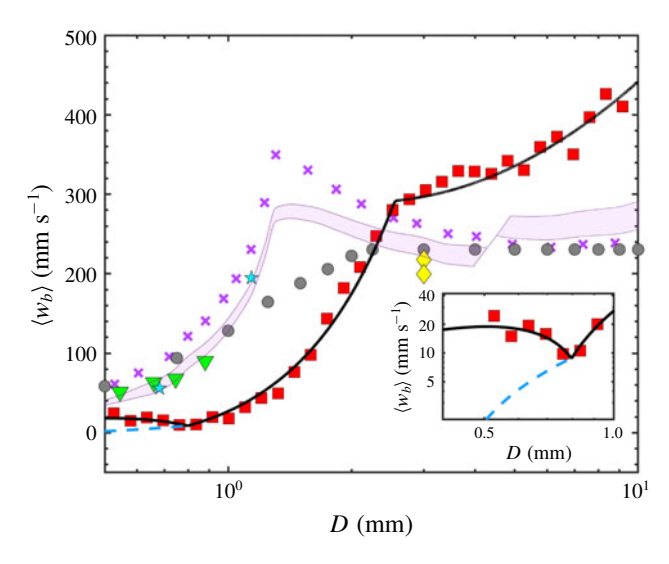


FIGURE 2. Mean bubble rise velocity $\langle w_b \rangle$ as a function of bubble diameter D in purified water (Clift, Grace & Weber 2005) (×); contaminated water (Clift et~al.~2005) (•); weak turbulence ($We \ll 1 < Eo$), including Aliseda & Lasheras (2011) (\P), Poorte & Biesheuvel (2002) (*) and Prakash et~al.~(2012) (•); and our experiments for intense turbulence (\blacksquare). Lines represent the model prediction for different conditions. The solid black line is calculated from our model, based on (4.3)–(4.5) at a high $\epsilon = 0.5~\text{m}^2~\text{s}^{-3}$. The purple shaded area represents the model prediction for weak turbulence ($We \ll 1 < Eo$) with $\epsilon = 1.3 \times 10^{-4} - 6 \times 10^{-3}~\text{m}^2~\text{s}^{-3}$ in clean water. The inset shows the same model prediction but using two lift models as shown in (4.8) and figure 3(b).

size D. That $\langle w_l \rangle$ is negative for small bubbles clearly shows that the nearby flows around small bubbles, on average, move downward. Velocity $\langle w_l \rangle$ increases, crosses zero and finally becomes positive as D grows, implying that the flows switch from hindering to assisting the rising motion of bubbles, which qualitatively explains why $\langle w_b \rangle$ exhibits such a dramatic change in figure 2. Different symbols in figure 3(a) correspond to different SRs used for selecting tracer particles around a bubble to estimate w_l . Note that very few particles can be triangulated within 1D away from the bubble centre as tracers close to a bubble can be easily shadowed by the bubble itself. Nevertheless, as flows in the close vicinity of a bubble (SR < 1D) are heavily modulated by the bubble motion, excluding these tracers from the statistics could help to avoid statistical bias. From SR = 1.5D to 3D, although with some variations, the observed trend of $\langle w_l \rangle$ seems to be consistent and insensitive to SR for bubbles with D > 1 mm. As SR also affects the number of tracer particles included for calculating $\langle w_l \rangle$, this consistent trend also implies well-converged statistics for bubbles with D > 1 mm. For small bubbles, results become sensitive to SR because of the insufficient number of tracers found within such a small SR.

Independent measurements of bubbles and surrounding tracers provide a consistent picture that bubbles of different sizes seem to be preferentially swept to regions with apparently opposing flow directions. The proposed mechanism of preferential sampling seems to be supported by the observed trend of $\langle w_l \rangle$. The surprising new finding is that bubbles do not always preferentially sample the downward flow side; the flow direction can be reversed for bubbles of large sizes. On the other hand, it may also imply that the vortex trapping idea does not apply to large bubbles, as vortex trapping

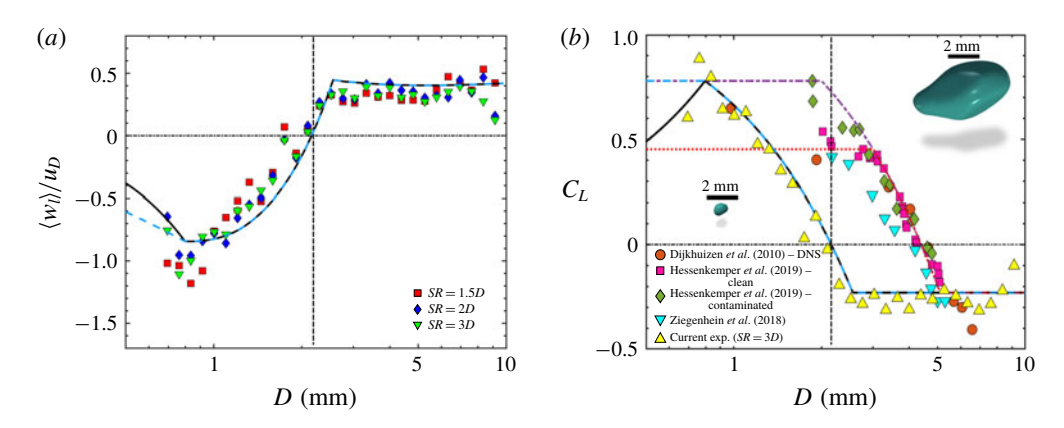


FIGURE 3. (a) The normalized mean vertical flow velocity $\langle w_l \rangle$ as a function of the bubble size D. Values of $\langle w_l \rangle$ are calculated based on three different SRs to find tracer particles around bubbles. (b) The lift coefficient C_L as a function of bubble size. Yellow triangles represent results obtained from $\langle w_l \rangle$ and $\langle w_b \rangle$ based on (4.4). Other symbols represent results from laminar shear flows for air—water systems, which were fitted with a piece-wise linear function for purified water (dotted red line, equation (4.6)) and contaminated water (dash-dotted purple line, equation (4.7)). Cyan dashed line and black solid line (4.9) represent the revised lift models for intense turbulence. The vertical dashed lines in both panels mark the transition point where turbulence-based W_e increases beyond 1. Two three-dimensional green blobs show the reconstructed three-dimensional shapes of small and large bubbles.

is often linked to the pressure gradient force without considering the lift force. As a result, bubbles of all sizes would end up being trapped in the centre of eddies with an overall reduced rise velocity, which does not agree with our observation.

To understand the reason behind the reversal of the preferential sampling direction, we start from the governing equation for finite-sized bubbles (Magnaudet & Eames 2000):

$$V_{b}(\rho_{b} + C_{A}\rho_{l})\frac{\mathrm{D}\boldsymbol{u}_{b}}{\mathrm{D}t} = \rho_{l}V_{b}C_{A}\frac{\mathrm{D}\boldsymbol{u}_{l}}{\mathrm{D}t} + V_{b}(\rho_{l} - \rho_{b})g\hat{\boldsymbol{e}}_{z} + \frac{\rho_{l}}{2}AC_{D}(\boldsymbol{u}_{l} - \boldsymbol{u}_{b})|\boldsymbol{u}_{l} - \boldsymbol{u}_{b}|$$
$$+ \rho_{l}C_{L}(\boldsymbol{u}_{l} - \boldsymbol{u}_{b}) \times (\nabla \times \boldsymbol{u}_{l}) - \frac{1}{2}V_{b}\nabla P_{w} + \boldsymbol{F}_{b}, \tag{4.1}$$

where ρ_l and ρ_b are the density of water and gas, respectively; V_b is the bubble volume; A is the projected area of a sphere with an equivalent volume of the bubble; u_l is the velocity of the unperturbed ambient flow taken at the centre of the bubble; F_b is the Basset history force; and C_D , C_L and C_A are the drag coefficient, lift coefficient and added mass coefficient, respectively.

Taking an ensemble average of both sides of (4.1) yields

$$0 = V_b(\rho_l - \rho_b)g\hat{\boldsymbol{e}}_z + \frac{\rho_l}{2}AC_D\langle(\boldsymbol{u}_l - \boldsymbol{u}_b)|\boldsymbol{u}_l - \boldsymbol{u}_b|\rangle + \rho_lC_L\langle(\boldsymbol{u}_l - \boldsymbol{u}_b) \times (\nabla \times \boldsymbol{u}_l)\rangle - \frac{1}{2}V_b\langle\nabla P_w\rangle$$
(4.2)

as $\langle Du_l/Dt \rangle = 0$ and $\langle Du_b/Dt \rangle = 0$ in homogeneous and isotropic turbulence, and the unsteady forces, including added mass and the Basset history force, become zero. In addition, the slip velocity between the two phases $\langle u_l - u_b \rangle$ is zero along the lateral

894 A20-8 A. K. R. Salibindla, A. U. M. Masuk, S. Tan and R. Ni



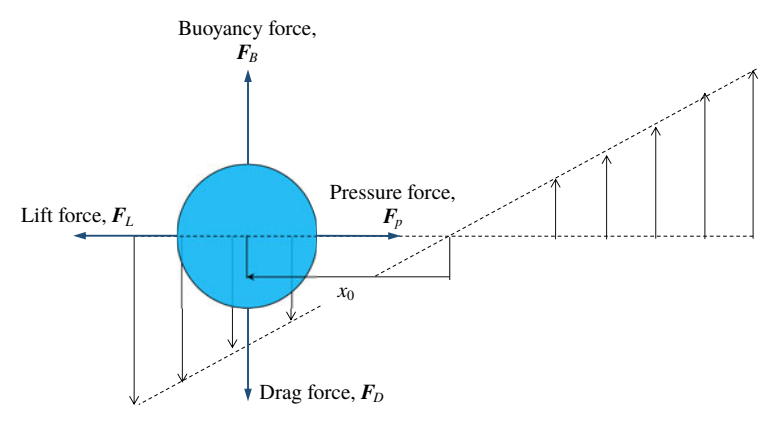


FIGURE 4. Schematic of a model for a bubble interacting with a uniform shear flow of constant shear rate (γ) to represent the ensemble-averaged bubble-eddy interaction. Four forces experienced by the bubble in (4.2) must balance with each other along two orthogonal directions.

directions and non-zero only along the vertical direction, which have been directly calculated from experiments and confirmed: $\langle u_l - u_b \rangle = \langle (w_l - w_b) \rangle = \langle w_l \rangle - \langle w_b \rangle$. The same principle applies to $\langle (u_l - u_b)|u_l - u_b|\rangle$, where only the vertical direction survives after the ensemble average: $\langle (u_l - u_b)|u_l - u_b|\rangle \approx (\langle w_b \rangle - \langle w_l \rangle)^2$.

The remaining two terms, the lift force and the pressure force, are associated with $\langle \nabla \times \boldsymbol{u}_l \rangle$. We assume that the interaction between a bubble and its surrounding flows can be modelled as a bubble interacting with local shear with shear rate of $\gamma = \langle \nabla \times \boldsymbol{u}_l \rangle = \mathrm{d}\langle w_l \rangle / \mathrm{d}x$, as depicted in figure 4. For the mean pressure force $\boldsymbol{F}_p = V_b \langle \nabla P_w / 2 \rangle$, solving the Poisson equation for pressure yields $\nabla P_w = \partial P_w(x) / \partial x = \rho_l \gamma^2 x \hat{\boldsymbol{e}}_x$. This indicates that the pressure force acts mainly along the horizontal direction $\hat{\boldsymbol{e}}_x$. For the same configuration, the ensemble average of lift $\boldsymbol{F}_L = \rho_l C_L(\boldsymbol{u}_l - \boldsymbol{u}_b) \times (\nabla \times \boldsymbol{u}_l)$ can be approximated as $\rho_l C_L(\langle w_l \rangle - \langle w_b \rangle) |\gamma| \hat{\boldsymbol{e}}_x$. In figure 4, it may seem that we picked the flow orientation so that the direction of \boldsymbol{F}_L , i.e. $\hat{\boldsymbol{e}}_x$, aligns with that of \boldsymbol{F}_p . But this is not a coincidence. As shown in the vector equation (4.2), out of four terms, buoyancy and the ensemble-averaged drag are along the vertical direction, $\hat{\boldsymbol{e}}_z$. The remaining two terms either have to share the same direction, or both of them have to be zero.

Following this argument, equation (4.2) can be written as two explicit equations along the vertical and lateral directions:

$$V_b(\rho_l - \rho_b)g\hat{\boldsymbol{e}}_z = \frac{1}{2}AC_D(\langle w_b \rangle - \langle w_l \rangle)^2\hat{\boldsymbol{e}}_z, \tag{4.3}$$

$$\rho_l C_L(\langle w_l \rangle - \langle w_b \rangle) |\gamma| \hat{\boldsymbol{e}_x} = \rho_l \gamma^2 x_0 \hat{\boldsymbol{e}_x}, \tag{4.4}$$

where x_0 represents the steady lateral location of bubbles within the shear flow (figure 4). The mean flow velocity $\langle w_l \rangle$ at this location can be calculated:

$$\langle w_l \rangle = \gamma x_0. \tag{4.5}$$

Positive or negative values of x_0 represent a bubble being swept to the upward or downward side of the shear, respectively. Shear rate γ scales with the velocity gradient of scale D, which can be related to the transverse second-order structure function $D_{NN} = 4(\epsilon D)^{2/3}/3$ in the form of $\gamma \sim 2(\sqrt{D_{NN}})/D = \sqrt{16/3}(\epsilon/D^2)^{1/3}$. This is where ϵ enters the model.

Equations (4.3)–(4.5) provide a simple model for the ensemble-averaged fluid and bubble velocity, which can be measured directly from our experiments. There are three unknowns in these three equations: C_D , C_L and x_0 . This indicates that these three unknowns can be linked to the measured results exactly without any fitting parameters. Solving these linear equations is straightforward. For example, from (4.4), $x_0 = C_L(\langle w_l \rangle - \langle w_b \rangle)/\gamma$. As shown in figure 4, once x_0 is known based on (4.5), the flow velocity experienced by bubbles is simply the velocity at location x_0 : $\langle w_l \rangle = \gamma x_0 = C_L(\langle w_l \rangle - \langle w_b \rangle)$.

This relationship suggests that C_L can be directly obtained from our measurements of $\langle w_l \rangle$ and $\langle w_b \rangle$. The results are shown as yellow triangles in figure 3(b). Only one SR, i.e. 3D, is used as $\langle w_l \rangle$ is not very sensitive to SR. For small bubbles (D < 2 mm), C_L is positive. As D increases, C_L continues to decrease until it reaches a negative value of -0.23. This transition indicates an inversion of the direction of this lateral lift

Similar lift direction inversion has also been observed in different types of flows: bubbles rising in laminar shear flows (Tomiyama *et al.* 2002; Dijkhuizen, van Sint Annaland & Kuipers 2010; Ziegenhein, Tomiyama & Lucas 2018; Hessenkemper, Ziegenhein & Lucas 2019) and bubbles in channel flows (Lu & Tryggvason 2008, 2013; Dabiri, Lu & Tryggvason 2013). Although neither of these two cases is turbulent, the mean shear is large enough to allow for the lift force to drive bubbles in the lateral directions. It was shown that small spherical bubbles tend to migrate towards the low-speed side whereas large deforming bubbles favour the opposing high-speed side (Tomiyama *et al.* 2002) because of the interaction between shear and bubble deformation (Lu & Tryggvason 2008; Adoua, Legendre & Magnaudet 2009). Although no mean shear exists in our system – flow is close to homogeneous and isotropic (Masuk *et al.* 2019*b*) – deformable bubbles could respond to the local shear created by turbulent eddies.

To compare C_L in the two systems more quantitatively, in figure 3(b), several recent datasets of C_L for bubbles rising in laminar shear flows (limited to air—water systems) (Dijkhuizen *et al.* 2010; Ziegenhein *et al.* 2018; Hessenkemper *et al.* 2019) are also shown. All results are consistent – C_L decays as D grows and eventually it becomes negative, which marks the direction reversal of the bubble transverse migration driven by lift. The transition location of C_L is believed to be associated with the buoyancy-induced deformation measured by E_D .

The inversion of C_L seems to occur at a larger D for the buoyancy-induced deformation than for the turbulence-driven cases. This difference can be attributed to different driving mechanisms of bubble deformation. In laminar shear flows, bubble deformation is only driven by buoyancy, measured by Eo. In our experiments, the lift inversion occurs when the bubble size increases from 2.2 mm (We = 0.71) to 2.7 mm (We = 1.00). As We crosses from below to above one, turbulence-induced bubble deformation becomes important. Note that this We does not account for bubble slip velocity or turbulence intermittency, which will only intensify the turbulence-induced deformation. Nevertheless, even without other compounding effects, this Weber number alone already indicates a possibility of an early lift inversion because of turbulence.

A. K. R. Salibindla, A. U. M. Masuk, S. Tan and R. Ni **894** A20-10

Other than the transition diameter, the trend of C_L from our experiments is very similar to that from laminar shear flows, both of which can be fitted with piece-wise linear functions. For laminar shear flows, given the difference between contaminated water and purified water, two separate fits can be provided:

$$C_{L} = \begin{cases} 0.45 & Eo < 1.25 \text{ (pure water),} \\ 1.453 - 0.9\sqrt{Eo} & 1.25 < Eo < 4, \\ -0.23 & 4 < Eo, \end{cases}$$

$$C_{L} = \begin{cases} 0.78 & Eo < 0.5 \text{ (contaminated),} \\ 1.453 - 0.9\sqrt{Eo} & 0.5 < Eo < 4, \\ -0.23 & 4 < Eo. \end{cases}$$

$$(4.6)$$

$$C_L = \begin{cases} 0.78 & Eo < 0.5 \text{ (contaminated),} \\ 1.453 - 0.9\sqrt{Eo} & 0.5 < Eo < 4, \\ -0.23 & 4 < Eo. \end{cases}$$
 (4.7)

In figure 3(b), equations (4.6) and (4.7) are shown as the red dotted line and purple dash-dotted line, respectively. The two equations are essentially the same; the only difference resides at the small-Eo limit. Note that these two equations are different from the proposed more complicated correlations of Legendre & Magnaudet (1998), Tomiyama et al. (2002), Hibiki & Ishii (2007) and Dijkhuizen et al. (2010). But the piece-wise linear correlations provide equally good fits for the data.

When turbulence becomes important ($We \gtrsim Eo$), the lift equation is adjusted to use We rather than Eo. Since many tracer particles are present in our system, bubble behaviours in our system should be similar to those in a contaminated case (equation (4.7)). Based on this argument, by adopting the same two limiting values of C_L from (4.7), a new equation of C_L for the turbulence-induced deformation is obtained:

$$C_L = \begin{cases} 0.78 & (2.671We^{3/5}) & We < 0.1\\ 1.25 - 1.608We^{3/5} & 0.1 < We < 0.9,\\ -0.23 & 0.9 < We. \end{cases}$$
(4.8)

The equation is shown as the cyan dashed line in figure 3(b). Equation (4.8) seems to agree with the data very well. Note that both (4.7) and (4.8) are piece-wise linear as a function of the bubble size D. Once Eo and We are used, the equations become dependent on \sqrt{Eo} and $We^{3/5}$ simply because $Eo \sim D^2$ and $We \sim D^{5/3}$.

The agreement between (4.8) and data is not perfect for small bubbles (D < 1 mm)because many bubbles do not have an adequate number of tracer particles within a small SR of 3D to calculate $\langle w_l \rangle$. Unfortunately, this range is crucial to constrain the behaviour of C_L for small bubbles, regarding which the community has not reached a consensus. The value of C_L could either be constant (Hibiki & Ishii 2007; Ziegenhein et al. 2018) or decrease to zero (Tomiyama et al. 2002). Equation (4.8) lists two possibilities of C_L for We < 0.1. These are that C_L either stays constant at 0.78 (cyan dashed line in figure 3b) or decreases from 0.78 to 0 linearly as D decreases from 0.8 mm to zero: $2.671 We^{3/5}$ (solid line). Both of these lines are also shown in figure 3(a).

Once C_L is known, the last unknown C_D can be determined from (4.3). Figure 5 shows the calculated C_D (blue circles) as a function of the bubble-scale Reynolds number, defined as $Re_b = (\langle w_l \rangle - \langle w_b \rangle)D/\nu$. For comparison, C_D from other experiments (Ishii & Chawla 1979; Ishii & Zuber 1979; Tomiyama *et al.* 1998; Loth 2008), including both clean and contaminated water, are also compiled in the

For small bubbles ($Re_b < 400$), our results agree very well with the data of Tomiyama et al. (1998) for bubbles rising in contaminated water (magenta triangles).

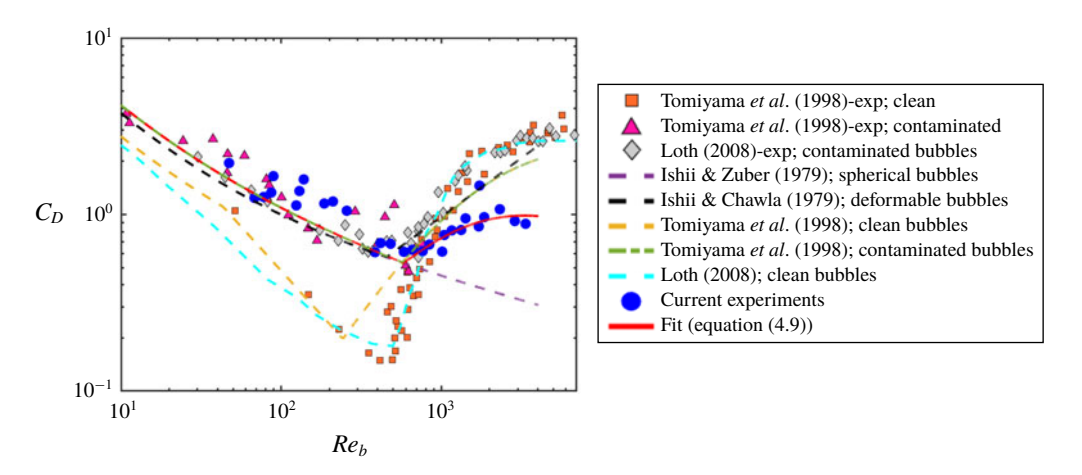


FIGURE 5. The drag coefficient for bubbles versus the bubble-size-based Reynolds number Re_b . Data obtained from our experiments are shown as blue circles. The proposed corrected drag model is shown as the red solid line (equation (4.9)). Previous works on bubbles rising in clean and contaminated quiescent water as well as different models are shown as symbols and lines, respectively.

As Re_b exceeds 400, C_D in intense turbulence becomes systematically lower. Since it occurs in the range of Re_b where pressure drag induced by bubble wake also significantly increases C_D , it may imply that turbulence modulates the bubble wake dynamics. The eddy turnover time $(\tau = \sqrt{4/3}(\epsilon^{-1/3}r^{2/3})) = 36.7$ ms for D = 4 mm) is much shorter than the wake shedding period based on the Strouhal number calculation $(\tau_w = 100 \text{ ms})$ for D = 4 mm (Lindt 1972; Brücker 1999). This suggests that it is challenging for a bubble to develop an established wake as the incoming flow direction keeps varying. It may explain the smaller C_D observed in intense turbulence compared to what has been found in a quiescent medium.

Here, we propose a corrected C_D curve based on the turbulence-based Weber number. This revised drag coefficient model is

$$C_D = \max(24/Re_b(1+0.15Re_b^{0.687}), \min(f(Eo), f(Eo)/We^{1/3})), \tag{4.9}$$

where f(Eo) = 8Eo/3(Eo+4). Although the formulation seems long, it is essentially a combination of three equations for three regimes: (i) solid-sphere model $C_D = 24/Re_b(1+0.15Re_b^{0.687})$ (Clift & Gauvin 1971) for small bubbles with slightly contaminated interfaces, (ii) the phase velocity model $C_D = f(Eo) = 8Eo/3(Eo+4)$ for large bubbles (Tomiyama *et al.* 1998) and (iii) our corrected model based on the Weber number We. For We < 1, C_D recovers the original formulation of 8Eo/3(Eo+4). For We > 1, drag for large Re_b is corrected to account for the modified wake effect. As shown in figure 5, this revised curve fits well to the measured results of C_D .

Based on (4.8) for C_L and (4.9) for C_D , we can finally explain the surprising behaviour of $\langle w_b \rangle$ shown in figure 2. First of all, the overall trend of this curve is determined primarily by the direction inversion of the lateral lift. Intense turbulence with a large ϵ brings in two effects: (i) a strong local velocity gradient, which effectively increases the contribution of lift and pressure gradient, and (ii) enhanced eddy velocity. The first effect can markedly change the mean bubble rise velocity as bubbles are swept to different sides of eddies, and the second effect amplifies the

magnitude change of $\langle w_b \rangle$. The behaviour of $\langle w_b \rangle$ for small bubbles (D < 1 mm) is shown in the zoomed-in inset of figure 2. Two lines correspond to two different C_L curves provided in (4.8). The solid line $(C_L = 2.671 We^{3/5} \ (We < 0.1))$ seems to agree better with $\langle w_b \rangle$.

Although our experiments were collected at a fixed ϵ , we found three prior works (Poorte & Biesheuvel 2002; Aliseda & Lasheras 2011; Prakash *et al.* 2012) involving different ϵ (ranging from 1.3×10^{-4} to 6×10^{-3} m² s⁻³) that can also be used to test the model. For $\epsilon < 0.1 \text{ m}^2 \text{ s}^{-3}$, We is much smaller than Eo for bubbles of size D = 0.5-3 mm. Therefore, for these cases, bubble deformation is primarily driven by buoyancy, and the turbulence effect is secondary. Moreover, in weak turbulence, We is not large enough to produce an early lift inversion. As a result, both C_L and C_D will recover that in a quiescent medium (red dotted line in figure 3(b) for C_L , and dashed green line in figure 5 for C_D). Taking both effects into consideration, the model prediction of $\langle w_h \rangle$ is shown in figure 2 as the purple shaded area (area covers the range of ϵ used in the three works), which passes through all the reported values. This area is indeed systematically lower than that for a quiescent medium by 20-40 %. This percentage change seems to be quite similar among these works despite a large range of ϵ used, which could be attributed to the saturation of $\langle w_l \rangle$. Since lift scales with γ and the pressure force scales with γ^2 , for small ϵ , lift is always dominant, pushing bubbles to the edge of an eddy and saturating $\langle w_l \rangle$ at the maximum eddy velocity, $\sim \gamma D/2$.

5. Summary

In summary, a new vertical water tunnel with a large energy dissipation rate was developed to study bubble dynamics in intense turbulence, in which turbulence-induced bubble deformation, measured by We, becomes close to or larger than buoyancy-induced deformation, quantified by Eo. Unlike other previous works conducted in weak turbulence ($Eo \gg We$), a surprising new behaviour of bubble rise velocity has been observed: within a small range of bubble sizes, bubble rise velocity transitions from an order of magnitude smaller to a factor of two larger than that in an otherwise quiescent medium.

Simultaneous measurements of dense tracer particles around bubbles show that flows around small bubbles move preferentially downward, hindering the rising motion of bubbles. Opposite upward flows are observed surrounding large bubbles, effectively increasing their rise velocity. This confirms the proposed preferential sampling mechanism that bubbles with different sizes tend to be swept to different regions in turbulence, rather than being trapped in the centre of eddies.

A model was derived by taking the ensemble average of both sides of the governing equation for bubble motion in turbulence. Since unsteady forces get averaged out in the process, only four forces, lift, buoyancy, drag and pressure gradient, are left in the equation. Two pairs of forces, buoyancy versus drag and lift versus pressure gradient, can be balanced along two orthogonal directions, which helps to utilize the measurable quantities, i.e. mean bubble and flow vertical velocity to estimate the drag and lift coefficients.

The lift coefficient shows clear direction inversion, similar to what has been extracted from experiments studying bubbles migrating in laminar shear flows. But in intense turbulence, $We \gtrsim Eo$, the transition occurs at a smaller bubble size when turbulence We switches from below to above one. The drag coefficient is also modified for large bubbles. Strong turbulence potentially affects the formation of bubble wakes,

which leads to a smaller drag coefficient. This effect also contributes to the enhanced rise velocity of bubbles. Finally, the model has also been tested on other datasets from previous works involving lower ϵ ; excellent agreement between the model predictions and the experimental results is observed without using any fitting parameters.

Acknowledgements

We acknowledge financial support from the National Science Foundation under award numbers 1705246 and CAREER-1653389.

Declaration of interests

The authors report no conflict of interest.

REFERENCES

- ADOUA, R., LEGENDRE, D. & MAGNAUDET, J. 2009 Reversal of the lift force on an oblate bubble in a weakly viscous linear shear flow. *J. Fluid Mech.* **628**, 23–41.
- ALISEDA, A. & LASHERAS, J. C. 2011 Preferential concentration and rise velocity reduction of bubbles immersed in a homogeneous and isotropic turbulent flow. *Phys. Fluids* **23** (9), 093301.
- BOETTCHER, E. J., FINEBERG, J. & LATHROP, D. P. 2000 Turbulence and wave breaking effects on air-water gas exchange. *Phys. Rev. Lett.* **85** (9), 2030.
- BRÜCKER, C. 1999 Structure and dynamics of the wake of bubbles and its relevance for bubble interaction. *Phy. Fluids* **11** (7), 1781–1796.
- CLIFT, R. & GAUVIN, W. H. 1971 Motion of particles in turbulent gas streams. *Brit. Chem. Engng* 16 (2–3), 229.
- CLIFT, R., GRACE, J. R. & WEBER, M. E. 2005 *Bubbles, Drops, and Particles*. Courier Corporation. DABIRI, S., LU, J. & TRYGGVASON, G. 2013 Transition between regimes of a vertical channel bubbly upflow due to bubble deformability. *Phys. Fluids* **25** (10), 102110.
- DIJKHUIZEN, W., VAN SINT ANNALAND, M. & KUIPERS, J. A. M. 2010 Numerical and experimental investigation of the lift force on single bubbles. *Chem. Engng Sci.* 65 (3), 1274–1287.
- ERN, P., RISSO, F., FABRE, D. & MAGNAUDET, J. 2012 Wake-induced oscillatory paths of bodies freely rising or falling in fluids. *Annu. Rev. Fluid Mech.* 44, 97–121.
- FRISCH, U. 1995 Turbulence: the Legacy of AN Kolmogorov. Cambridge University Press.
- HESSENKEMPER, H., ZIEGENHEIN, T. & LUCAS, D. 2019 Contamination effects on the lift force of ellipsoidal air bubbles rising in saline water solutions. *Chem. Engng J.* (in press).
- HIBIKI, T. & ISHII, M. 2007 Lift force in bubbly flow systems. *Chem. Engng Sci.* **62** (22), 6457–6474. HINZE, J. O. 1955 Fundamentals of the hydrodynamic mechanism of splitting in dispersion processes. *AIChE J.* **1** (3), 289–295.
- ISHII, M. & CHAWLA, T. C. 1979 Local drag laws in dispersed two-phase flow. NASA Sti/Recon Tech. Rep. N 80.
- ISHII, M. & ZUBER, N. 1979 Drag coefficient and relative velocity in bubbly, droplet or particulate flows. *AIChE J.* **25** (5), 843–855.
- KAWASE, Y. & MOO-YOUNG, M. 1990 Mathematical models for design of bioreactors: applications of: Kolmogoroff's theory of isotropic turbulence. *Chem. Engng J.* **43** (1), B19–B41.
- KOLMOGOROV, A. 1949 On the breakage of drops in a turbulent flow. *Dokl. Akad. Nauk. SSSR* 66, 825–828.
- LEGENDRE, D. & MAGNAUDET, J. 1998 The lift force on a spherical bubble in a viscous linear shear flow. J. Fluid Mech. 368, 81–126.
- LEWANDOWSKI, B., FERTIG, M., KREKEL, G. & ULBRICHT, M. 2018 Analysis of wake structures in bubbly flows using particle image velocimetry (PIV). In 7th European Young Engineers Conference Monograph, Warsaw University of Technology, Faculty of Chemical and Process Engineering, Warsaw, pp. 367–375.

- 894 A20-14 A. K. R. Salibindla, A. U. M. Masuk, S. Tan and R. Ni
- LINDT, J. T. 1972 On the periodic nature of the drag on a rising bubble. *Chem. Engng Sci.* 27 (10), 1775–1781.
- LIU, Z., ZHENG, Y., JIA, L. & ZHANG, Q. 2005 Study of bubble induced flow structure using PIV. Chem. Engng Sci. 60 (13), 3537–3552.
- LOHSE, D. 2018 Bubble puzzles: from fundamentals to applications. Phys. Rev. Fluids 3 (11), 110504.
- LOISY, A. & NASO, A. 2017 Interaction between a large buoyant bubble and turbulence. *Phys. Rev. Fluids* 2 (1), 014606.
- LOTH, E. 2008 Quasi-steady shape and drag of deformable bubbles and drops. *Intl J. Multiphase Flow* **34** (6), 523–546.
- LU, J. & TRYGGVASON, G. 2008 Effect of bubble deformability in turbulent bubbly upflow in a vertical channel. *Phys. Fluids* **20** (4), 040701.
- Lu, J. & Tryggvason, G. 2013 Dynamics of nearly spherical bubbles in a turbulent channel upflow. J. Fluid Mech. 732, 166–189.
- MAGNAUDET, J. & EAMES, I. 2000 The motion of high-Reynolds-number bubbles in inhomogeneous flows. *Annu. Rev. Fluid Mech.* **32** (1), 659–708.
- MASUK, A. U. M., SALIBINDLA, A. & NI, R. 2019a A robust virtual-camera 3D shape reconstruction of deforming bubbles/droplets with additional physical constraints. *Intl J. Multiphase Flow* **140** (28), 103088.
- MASUK, A. U. M., SALIBINDLA, A., TAN, S. & NI, R. 2019b V-onset (vertical octagonal noncorrosive stirred energetic turbulence): a vertical water tunnel with a large energy dissipation rate to study bubble/droplet deformation and breakup in strong turbulence. *Rev. Sci. Instrum.* 90 (8), 085105.
- MATHAI, V., LOHSE, D. & SUN, C. 2020 Bubble and buoyant particle laden turbulent flows. *Annu. Rev. Condens. Matter Phys.* 11, 529–559.
- MAZZITELLI, I. M., LOHSE, D. & TOSCHI, F. 2003 On the relevance of the lift force in bubbly turbulence. *J. Fluid Mech.* 488, 283–313.
- MERCADO, J. M., PRAKASH, V. N., TAGAWA, Y., SUN, C., LOHSE, D. & (INTERNATIONAL COLLABORATION FOR TURBULENCE RESEARCH) 2012 Lagrangian statistics of light particles in turbulence. *Phys. Fluids* **24** (5), 055106.
- MOUGIN, G. & MAGNAUDET, J. 2001 Path instability of a rising bubble. *Phys. Rev. Lett.* 88 (1), 014502.
- POORTE, R. E. G. & BIESHEUVEL, A. 2002 Experiments on the motion of gas bubbles in turbulence generated by an active grid. *J. Fluid Mech.* **461**, 127–154.
- PRAKASH, V. N., TAGAWA, Y., CALZAVARINI, E., MERCADO, J., TOSCHI, F., LOHSE, D. & SUN, C. 2012 How gravity and size affect the acceleration statistics of bubbles in turbulence. *New J. Phys.* **14** (10), 105017.
- RISSO, F. 2018 Agitation, mixing, and transfers induced by bubbles. *Annu. Rev. Fluid Mech.* **50**, 25–48.
- SHE, Z., JACKSON, E. & ORSZAG, S. 1990 Intermittent vortex structures in homogeneous isotropic turbulence. *Nature* **344** (6263), 226–228.
- SPELT, P. D. M. & BIESHEUVEL, A. 1997 On the motion of gas bubbles in homogeneous isotropic turbulence. *J. Fluid Mech.* 336, 221–244.
- SRIDHAR, G. & KATZ, J. 1995 Drag and lift forces on microscopic bubbles entrained by a vortex. *Phys. Fluids* 7 (2), 389–399.
- TAN, S., SALIBINDLA, A., MASUK, A. U. M. & NI, R. 2019 An open-source Shake-the-Box method and its performance evaluation. In 13th International Symposium on Particle Image Velocimetry ISPIV 2019.
- TAN, S., SALIBINDLA, A., MASUK, A. U. M. & NI, R. 2020 Introducing OpenLPT: new method of removing ghost particles and high-concentration particle shadow tracking. *Exp. Fluids* **61** (2), 47.
- TOMIYAMA, A., KATAOKA, I., ZUN, I. & SAKAGUCHI, T. 1998 Drag coefficients of single bubbles under normal and micro gravity conditions. *JSME Intl J. B* 41 (2), 472–479.
- TOMIYAMA, A., TAMAI, H., ZUN, I. & HOSOKAWA, S. 2002 Transverse migration of single bubbles in simple shear flows. *Chem. Engng Sci.* 57 (11), 1849–1858.

- WANG, L. & MAXEY, M. R. 1993 The motion of microbubbles in a forced isotropic and homogeneous turbulence. *Appl. Sci. Res.* **51** (1–2), 291–296.
- WOOLF, D. K. 1997 Bubbles and their role in gas exchange. In *The Sea Surface and Global Change*. Cambridge University Press.
- ZIEGENHEIN, T., TOMIYAMA, A. & LUCAS, D. 2018 A new measuring concept to determine the lift force for distorted bubbles in low morton number system: results for air/water. *Intl J. Multiphase Flow* 108, 11–24.